

Robust Closed-Loop Control on a 2D-High-Lift-Device

Notger Heinz and Rudibert King

Chair of Measurement and Control, Department of Process and Plant Technology,
Technische Universität Berlin Hardenbergstr. 36a, 10623 Berlin, Germany

Frank Haucke and Wolfgang Nitsche

Chair of Aerodynamics, Department of Aeronautics and Astronautics,
Technische Universität Berlin
Marchstr. 12, 10587 Berlin, Germany

This work shows the application of robust closed-loop strategies on a 2D high-lift configuration. The aim is to control the amount of lift achieved, instead of maximising that amount as it is usually done with open-loop set-ups. A way to model a 2D high-lift-device will be outlined, based on linear black-box-models of the lift as a function of the actuation amplitude. This model will be examined with respect to needed complexity and sensitivity to experimental parameters. In an experimental implementation the disturbance rejection and tracking capability of a synthesized closed-loop-controller will be shown and its possible use in aviation pointed out.

NOMENCLATURE

symbol	unit	description
b	mm	span width
C	—	controller transfer function
c_f	mm	flap chord length
c_m	mm	mean chord length
c_μ	—	momentum coefficient
c_p	—	pressure coefficient
$c_p(x)$	—	local pressure coefficient
C_D	—	drag coefficient
C_L	—	lift coefficient
C_s	—	optimization variable in controller synthesis
DC_e	%	duty cycle of excitation
e	$\frac{N}{m}$	tracking error
f_e	Hz	frequency of excitation
$F_e^+ = \frac{f_e \cdot c_f}{u_\infty}$	—	reduced frequency of excitation
H_∞	—	infinity-norm
I	—	identity matrix
L	N	lift force
l	$\frac{N}{m}$	line force of lift
l_{ref}, l_e, l_{mean}	$\frac{N}{m}$	reference, estimated and mean line lift force, respectively
M	—	measurement matrix
P	—	plant model transfer function
P_n	—	nominal plant model
P_u	—	uncertain plant model
R	—	covariance matrix

Re_c	—	chord Reynolds number
u	V	actuation voltage
u_-, u_+	V	lower and upper actuation voltage in PRBS-perturbation experiments
u_{max}	V	maximum actuation voltage
u_∞	$\frac{m}{s}$	incident velocity
s	$\frac{1}{s}$	Laplace variable
t	s	time
T	s	periodic time
U	—	left singular value decomposition matrix
V	—	right singular value decomposition matrix
\bar{V}	—	reduced eigenvector matrix
\dot{V}_N	$\frac{l_N}{min}$	normalized volume flow rate
W_1	—	pre-shaping weight for controller synthesis
W_2	—	post-shaping weight for controller synthesis
w_i	—	weight for uncertainty modeling
x, x_f	mm	position along the chord length and flap chord length resp.
X	—	principal axis transformation of measurement data
α	deg	angle of attack
β	deg	blowing angle
Δ	—	uncertain element
Δp_i	$\frac{N}{m^2}$	pressure difference on the i-th segment
δ_f	deg	flap deflection angle
κ_1	—	constant parameter in plant description
κ_2	—	constant parameter in plant description
ϕ	rad	phase angle
φ	—	parameter vector in parameter identification
Σ_r, Σ	—	(reduced) singular value matrix
σ	—	singular value
τ_d	s	derivative time constant
ω	rad/s	angular frequency
ω_c	rad/s	critical angular frequency

I. INTRODUCTION

Active flow control (AFC) has been shown to enhance performance of airfoils and high-lift set-ups for numerous configurations [7],[9].

Various methods of influencing the flow have been implemented; from flaperons to synthetic jets [28], suction and blowing devices [17], plasma actuators [8] and trapped vorticity actuators [6]. All were able to influence the flow beneficially, mostly enhancing lift and delaying stall. Thus, AFC has been proven to be an option that is worth to be considered when designing an airplane [14],[4],[26].

This work focuses on a special application, the high-lift configuration, which is necessary for landing and – to a lesser extent – take-off, where a high lift at angles of attack in the linear lift polar regime – where the lift depends on the angle of attack in a linear fashion – is desired. These angles would be well below the maximum angles of attack, where flow separation would occur. The airplane industry has fared quite well with passive systems that avoid flow separation at these angles of attack sometimes at the expense of mechanically complex flap systems. Still, there is room to improve the performance, to widen the range of possibilities and to reduce the mechanical complexity. This paper shows one way to apply AFC to enhance the lift generated by a high-lift configuration that actually uses a normally separated flow and partly or fully reattaches it. This opens up new degrees of freedom in airfoil design, enabling smaller flaps, higher flap angles, smaller number of total flaps, even totally new flap or airfoil types [5]. Moreover, new landing approach trajectories will be possible.

In a real-world environment, such a system would have to work self-sustaining and autonomously and it would be subject to disturbances (gusts), uncertainties (flow behaviour not precisely known, aging of

parts or material, etc.) and varying environmental conditions (temperature, humidity, surrounding pressure). While in well-defined environments – such as in wind tunnel studies – open-loop has its merits, in a real-world environment one needs a closed-loop concept to account for these factors. Closed-loop systems can change the actuation in nearly real-time such that disturbances are rejected, uncertainties can be ignored and varying environmental conditions can be compensated for [16],[24],[15],[13].

In the history of AFC, open-loop was the prevalent way experiments were done. From Prandtl's boundary layer control [25] with high actuation costs to modern AFC-devices with their pulsed actuation [9],[20], the huge bulk of works was about experimental set-ups with new sets of actuators, whose efficiency and effectiveness was measured. Feed-back approaches remained the rare exception until recently.

Becker et al. [2] showed that model-free slope seeking controllers could enhance the performance of airfoils even beyond what open-loop actuation could achieve. Tian et al. [30] showed that adaptive online identification of an ARMARKOV-model could be used to suppress disturbances on a 2D-airfoil and Ciuryla et al. [5] implemented a black-box-model-based closed-loop approach to achieve a flight trajectory control by means of wing-tip actuation. Tchieu et al. [29] showed the applicability of low-order vortex-based models and Luchtenburg et al. [19] of low-order Galerkin systems for closed-loop control of a 2D-flow. Brzozowski et al. [3] applied closed-loop control to suppress disturbances on a free moving UAV airfoil. Williams et al. [32] considered closed-loop control in unsteady flows and Heinz et al. [12] for an industrial high-lift device.

This work follows the line of linear black-box-modeling and robust control theory to design a controller that does not aim at achieving the maximum lift possible at a given angle, but rather a commanded lift, commandable within the boundaries of the physical reality. Though the underlying problem is inherently non-linear in nature, a linear approach will be pursued and shown to be sufficient to achieve a good performance and disturbance suppression.

The paper is organized as follows: Section 2 gives a description of the experimental set-up and the measurement characteristics. It is followed by black-box modeling, examination of the necessary order of models obtained to adequately describe the flow dynamics and eventually controller synthesis in section 3. This leads to the validation of the controller in the experiment in section 4. On a brief side-note, we will review the requirements for sensors in the set-up in section 5. Section 6 finally summarizes the findings.

II. EXPERIMENTAL SET-UP AND MODEL DESCRIPTION

All experiments were carried out in a closed-loop wind tunnel that is shown in Fig. 1 schematically. The drive power of this facility is 500 kW and flow velocities of up to 50 m/s are possible. The nozzle had a contraction ratio of 6.25:1 and the free stream intensity of turbulence was 0.2%. The test section consists of four modular parts with an area cross-section of $2\text{ m} \times 1.41\text{ m}$ and a total length of 10 m.

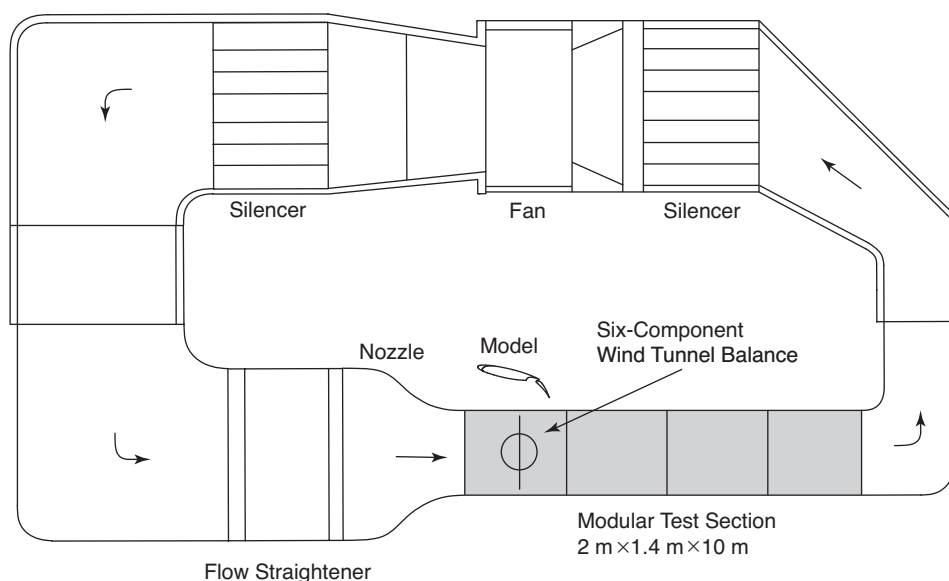


Figure 1: Low speed wind tunnel, Institute of Fluid Mechanics and Engineering Acoustics, Technische Universitaet Berlin.

A six-component wind tunnel balance was located underneath the first module of the test section for measuring all forces with an accuracy of 0.1% and moments with an accuracy of up to 0.3% simultaneously.

Wind-Tunnel Model

For the experimental investigations, a two dimensional high lift configuration consisting of a main element and a single slotted trailing edge flap was used. In clean configuration this model had a transonic body shape and a profile depth of $c = 600 \text{ mm}$. This model was identical in profile shape with the DLR F15 model [31] of the German Aerospace Center. The aspect ratio was 2.58. A very stiff beam construction connected the model with a six-component balance that was placed underneath the test section. The wing's mounting was encased by additional vertical side walls in order to avoid additional drag forces of the vertical beams and to reduce the influence of the wind tunnel walls' boundary layer. That is why the span width of the model measured only $b = 1.55 \text{ m}$ instead of 2 m (see Fig. 2). To avoid lateral pressurization between the wing's lower and upper side the distances between the ends of the model and the side walls were very small ($\approx 0.1 \text{ mm}$) but it was ensured that the rotatory motion was still contactless.

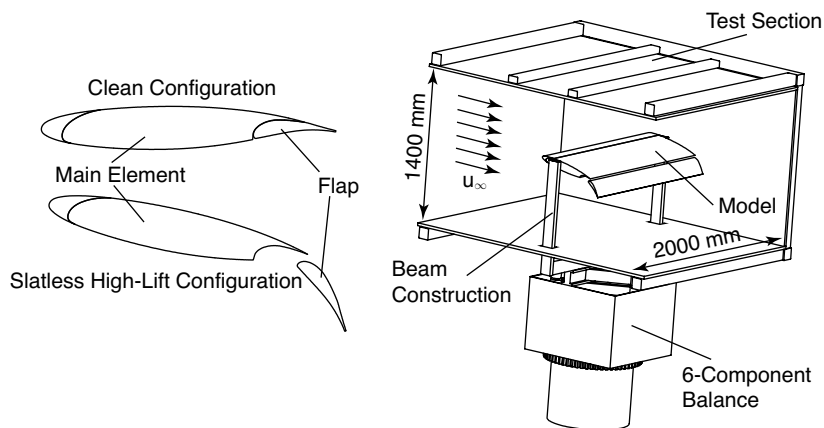


Figure 2: Experimental set-up.

All forces and moments were measured directly from the balance system and were used for determining the aerodynamic coefficients. In addition, the pressure distribution in the mid section of the main element and at three span-wise locations on the flap (see Fig. 4) were acquired. Therefore, miniature pressure sensors were used, 32 for the main wing and 32 for the trailing edge flap. The accuracy for these sensors was $\pm 1\%$. Most of the measurement equipment was integrated within the main element to reduce the supply and data lines which had to be led through the mounting, along the beam construction, out of the test section. Angle of attack and flap deflection angle could be changed by computer controlled stepping motors with an accuracy of $\pm 0.1^\circ$. In order to set up flap gap and flap overlap, special flap holders were used to obtain the desired values.

All data in- and output was handled via a digital signal processor (DSP, dSpace DS1005) and 14-bit A/D and D/A-converters, respectively. The DSP's sampling rate was at 4 kHz. The balance signals were filtered by an analog 6th-order low-pass-filter before being sampled and digitized.

For these measurements, maximum flow velocities of up to $u_\infty = 30 \text{ m/s}$ were used. The corresponding Reynolds numbers reached values of about $1.2 \cdot 10^6$. This maximum Reynolds number might be too low to assure a fully developed turbulent flow around the model for each variation of angle of attack (AoA), flap deflection angle, flap gap or flap overlap. Therefore, small tapes, placed at positions near the leading edges of the main element and of the flap, were used to force the laminar to turbulent transition process along the span-wise direction. The width and the thickness of these tapes were varied in order to find the best set-up to avoid laminar flow separation but keeping the impact on the flow as small as possible during the measurements. The flow state was determined by interpreting the pressure distribution for each angle of attack (AoA) during each lift polar. For sudden separation starting from the leading edge of an airfoil without any indication at the previous smaller AoA or significant hysteresis characteristics for the reversed lift polar it can be assumed that the flow state is laminar. But if a turbulent flow separates, it is characterized by starting the separation from the trailing edge of an airfoil and the recirculation area enlarges upstream with increasing AoA. In this case,

hysteresis behavior is not visible or marginal. One tape set-up was found that was capable of generating a turbulent flow and preventing a laminar leading edge separation for all tested configurations. On the main element, two tapes ($2 \text{ mm} \times 0.05 \text{ mm}$) located at $x/c = 0\%$ and $x/c \approx 2.5\%$ and on the flap two tapes ($1 \text{ mm} \times 0.05 \text{ mm}$) placed at $x_f/c_f = 0\%$ and $x_f/c_f \approx 5\%$ were finally used.

Actuator System

In general, one actuator segment consists of three main components, a supply of compressed air, a fast switching solenoid valve (Festo) and a chamber (see Fig. 3). Due to a square wave supply voltage (see Fig. 3), which was controlled by the DSP, each fast switching solenoid valve was opened and closed cyclically with the desired frequency and duty cycle. This generated a pulsed flow within the connecting pipe to the actuator chamber. The purpose of the chamber was to transform the pulsed flow, originating from the valve, into a pulsed jet with the desired velocity profile at the actuator outlet. The spatial and temporal uniformity of the jet along the slot was also desired in order to realize an almost consistent impact of the jet on the local flow field. The amplitude of the pulsed jets was set by the pressure within the compressed air duct which was controlled by electronic proportional pressure regulators (Festo) outside of the test section. In addition an electronic volume flow rate meter was used in order to determine the consumption of compressed air and the momentum coefficient c_{μ} .

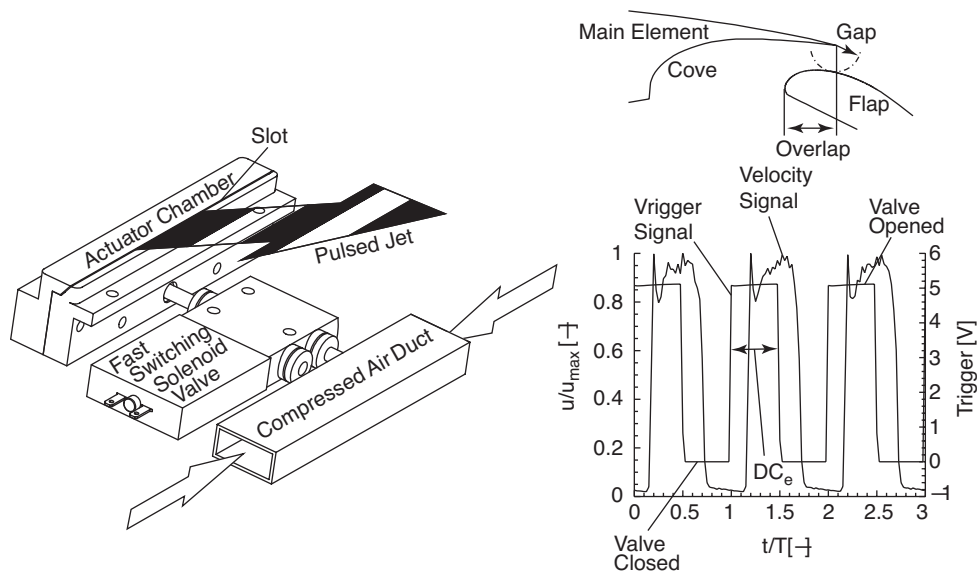


Figure 3: Components of the actuator system and parameters important for AFC; $T = 1/75 \text{ s}$.

Based on previous investigations [11],[10] a new actuator configuration was used for the experiments described in this contribution. In flow direction at two locations on the flap, at $x_f/c_f = 0.2$ and at $x_f/c_f = 0.5$, the flow was excited with actuators mentioned above. In span-wise direction the actuator segments were staggered as it is shown in Fig. 4. In each case the geometrical blowing angle was about $\beta \approx 30^\circ$ with respect to the local tangent surface. Altogether 13 actuator segments, seven located at $x_f/c_f = 0.2$ and six at $x_f/c_f = 0.5$, were used for active flow control on this flap. Each actuator slot had a width of about $2.4 \cdot 10^{-3} \cdot c_f$ and a length of about $0.53 \cdot c_f$. For the measurements described in this paper all actuators operated with the same frequency, duty cycle and pipe pressure.

Time-Averaged Characteristics

The sample results for time-averaged characteristics were obtained for a chord Reynolds number of about $Re_c = 1 \cdot 10^6$. The forces and moments measured by the six-component balance were corrected by a standard wind tunnel correction [1]. Pulsed blowing could generate large scaled flow structures that

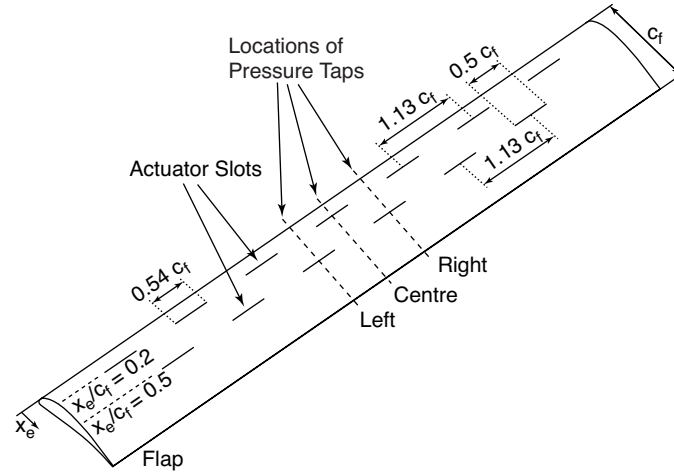


Figure 4: Actuator integration into the flap.

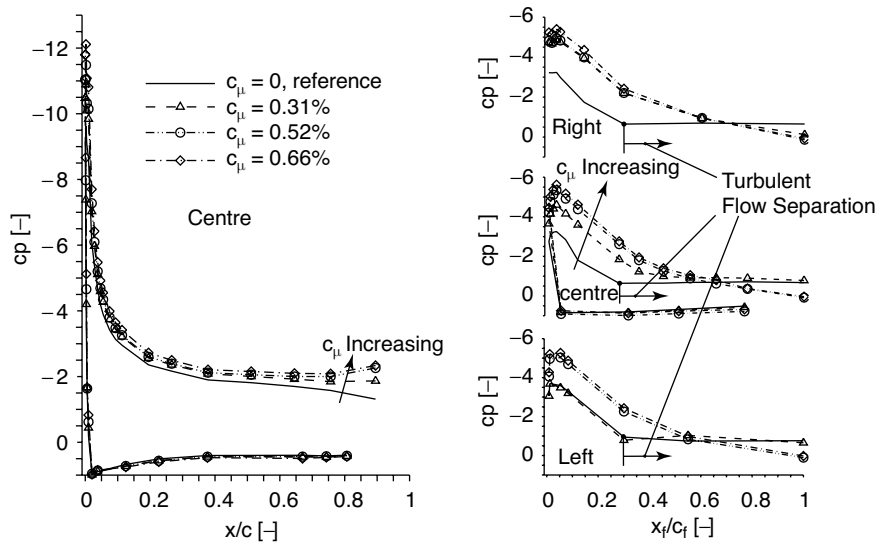


Figure 5: Time-averaged characteristics for $f_e = 75$ Hz, $DC_e = 50\%$: pressure distributions at $\alpha = 5^\circ$ and $\delta_f = 45^\circ$. Left: Main wing. Right: Flap.

are capable to amplify turbulent mixing and to avoid turbulent flow separation on the flap. Figure 5 shows some exemplary pressure distributions in the center of main element and at three different span-wise locations on the flap. For the reference case, AFC was switched off and turbulent flow separation on the flap occurred at $x_f/c_f \approx 0.3$ for all three span-wise locations on the flap. Excitation parameters were then set to $f_e = 75$ Hz, $DC_e = 50\%$ while changing the momentum coefficient c_μ . For increasing momentum of the pulsed jets the pressure level was lowered on the upper side of the flap and of the main element as well. Compared to the reference case without AFC this led to increasing lift coefficients in the linear region of the lift polars, see Fig. 6. The maximum AoA was slightly reduced for increasing momentum coefficients and maximum lift enhancement was about $\Delta C_L \approx 0.54$ for this setting.

III. BLACK-BOX MODELING AND CONTROLLER SYNTHESIS

A typical landing scenario would take place at a certain set of angles α and δ_f . A closed-loop control of lift for landing would then only need to work at this set of angles and, thus, a modeling of the aerodynamical behaviour is only necessary around these operating points, admitting for disturbances in the actual angle-of-attack created by gusts. In this experiment, we chose the angles of attack of four to six degrees as our operation points, staying well into the linear part of the lift polar diagram.

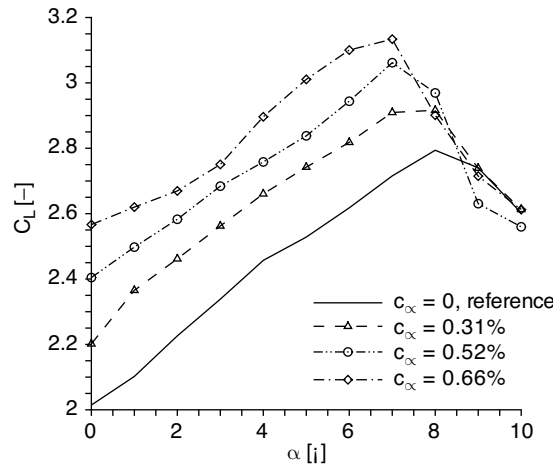


Figure 6: Time-averaged characteristics for $f_e = 75 \text{ Hz}$, $DC_e = 50\%$: lift polars, $\delta_f = 45^\circ$.

Black-Box Modeling

Before beginning with the modeling process, one has to ascertain that the sensor information available is a good measure for what one wants to control. In our case, we wanted to control the lift. However, in free flight it will be impossible to measure the lift. Moreover, the balance was not fit for time-resolved measurements due to strong eigendynamics that were superimposing the measurements of the aerodynamic forces. Therefore, the data given above were obtained by applying an averaging procedure over twenty seconds. Thus, the pressure sensors on the wing were the only sensor data usable for the closed-loop control. This sensor data was numerically integrated along the center-line of the wing using trapezoidal rule to derive a line-force l , representing the total lift force L . l would then be our control variable.

Figure 7 shows that l obtained from the pressure sensors is a reasonably good measure for the lift generated. It is non-linearly linked to the lift force L , but monotonous such that one can state that, as long as l rises due to increased actuation, the actual lift force rises as well. With the help of a look-up-table, we were able to establish an unambiguous connection between our measured line-force and the true lift force generated at the balance for every given operating point, so that $l \propto L$.

To synthesize a linear robust controller, a linear model of the systems dynamics is needed. In case of a non-linear system behaviour – as existing here – local linear models are identified to describe the local system dynamics in the vicinity of certain operating points, e.g., certain α and actuation levels. To denote actuation levels, the standard control engineering symbol u is used, which should not be

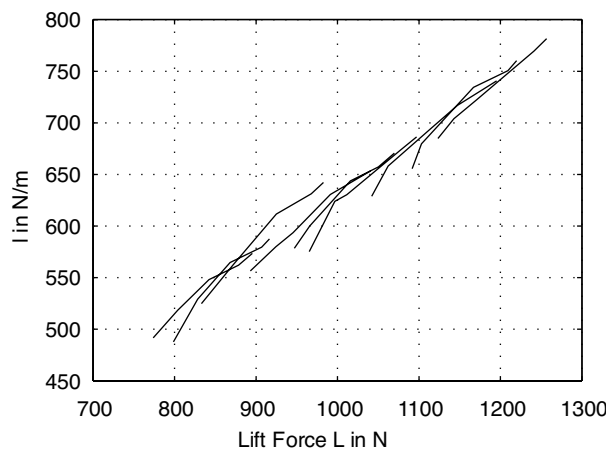


Figure 7: Line-force of lift l versus balance force L for different α and Re_c numbers measured with three seconds averaging time for a determination of L and l .

mistaken for velocity signals, c.f. u_∞ . These local linear models constitute a model family, out of which one representative – the so-called nominal model – is chosen to synthesize the controller on. To show stability and robustness, this nominal model is then enhanced with a modeled uncertainty, so that the so-called uncertain model obtained encompasses all the identified dynamics that were part of the original model family.

In order to obtain the local linear models of the system dynamics, forced experiments were conducted. These exploited a pseudo-random binary signal [18] (PRBS) to supply the actuators with varying pressure. Duty-cycle and frequency were fixed at values given in Table 1, corresponding to settings that have shown good results in preliminary tests, c.f. Fig. 6.

Table 1: Overview over the experimental parameters.

DC_e	50%
f_e	75 Hz
Re_c	10^6
δ_f	45°

Figure 8 shows one exemplary time-resolved plot of the excitation signal and the system answer, the line-force of lift l .

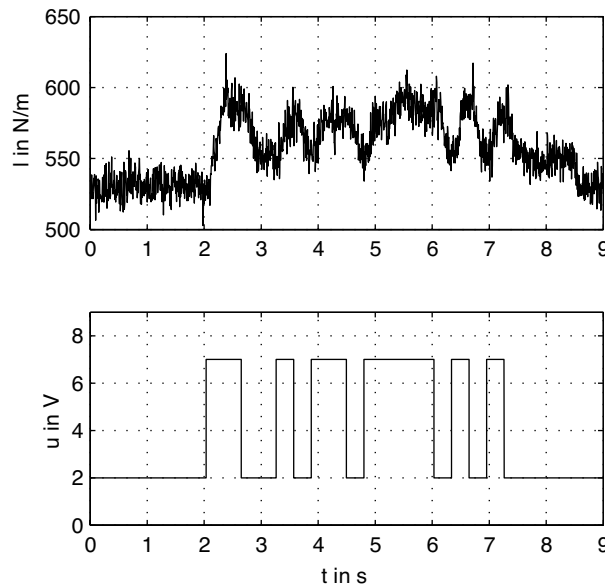


Figure 8: PRBS-perturbation experiment at $\alpha = 5^\circ$, $\delta_f = 45^\circ$, $Re_c = 10^6$, showing the actuation variable to switch between $u_- = 2V$ and $u_+ = 7V$ and the measured line force of lift l . The actuation variable shows the pressure feeding the solenoid valves, which themselves operate at $f_e = 75$ Hz.

A linear black-box model was fitted to this data to model the system behaviour with respect to the excitation. Figure 9 shows a comparison of measured and simulated line force for the model obtained for $\alpha = 5^\circ$, $\delta_f = 45^\circ$ and $Re_c = 10^6$.

This procedure was repeated for different excitation values at different angles α . It was found that α had negligible impact on the system dynamics, with different α giving very similar fits for the same PRB-signals. The entirety of the models of different orders comprise a model family, as shows in Fig. 10. Here, the plot of the frequency-dependent gain and the frequency-dependent phase shift of the output signal l towards the actuation signal u is given as a Bode plot. The black highlighted model is the nominal model, see below, which was chosen to synthesize the controller. The choice was based on this model being a mean representative of all identified system behaviours.

Though the models do not cover every aspect of the dynamics, notably not the non-linearities, different dead-times, time-dependent parameters or hysteresis effects, they are reasonably good at

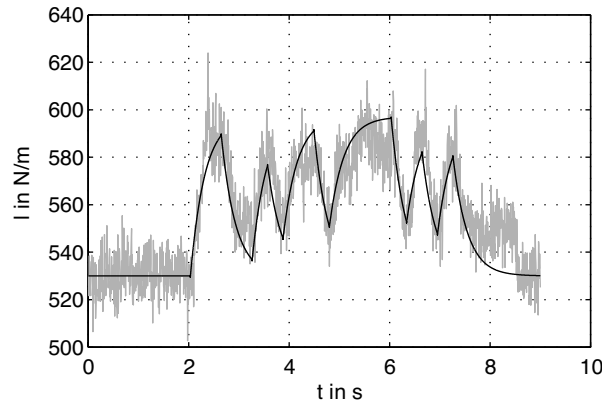


Figure 9: Identified model (black) for a PRBS-perturbation experiment at $\alpha = 5^\circ$, $\delta_f = 45^\circ$, $Re_c = 10^6$ (grey).

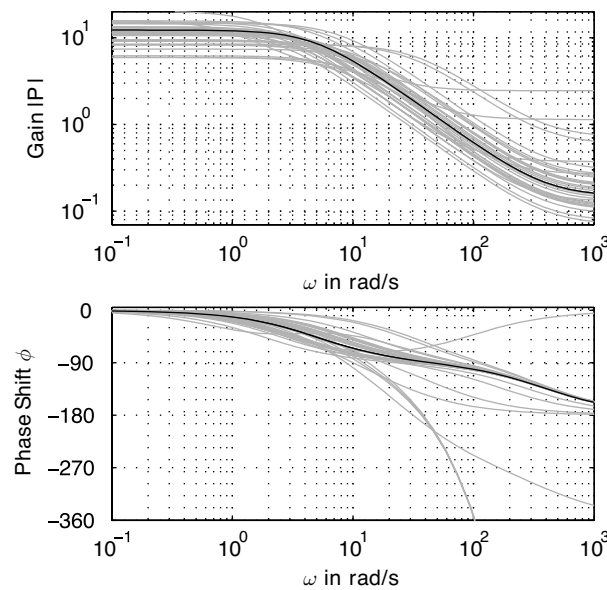


Figure 10: Identified model family for various PRBS-perturbation experiments (grey) and the nominal model (black) used for controller synthesis.

describing the main dynamics. A closed-loop controller can cope with a degree of uncertainty and, thus, all the effects not modelled are viewed as uncertainties. Part of them are reflected in the model family (different gains at different operating points, different bandwidths), part of them are simply ignored and left over for the closed-loop controller to cope with (different dead-times, time-varying characteristics, hysteresis effects).

For most of the experiments, a first-order differential equation was enough to approximate the observed system output. This leads to a lead-lag-behaviour, with the Laplace-transformed form $P = \frac{\tau_d s + k_1}{s + k_2}$. P is known as a transfer function.

Figure 11 shows that the quality of the fit does not improve with higher model orders. The fit is here defined as

$$fit = 100 \times (1 - \|l_e - l\|_2 / \|l - l_{mean}\|_2) \% \quad (1)$$

with l_e being the estimated lift-force calculated from the identified model based on the actuation sequence from the PRBS-perturbation experiment and l_{mean} being the mean value of the measured l for said experiment.

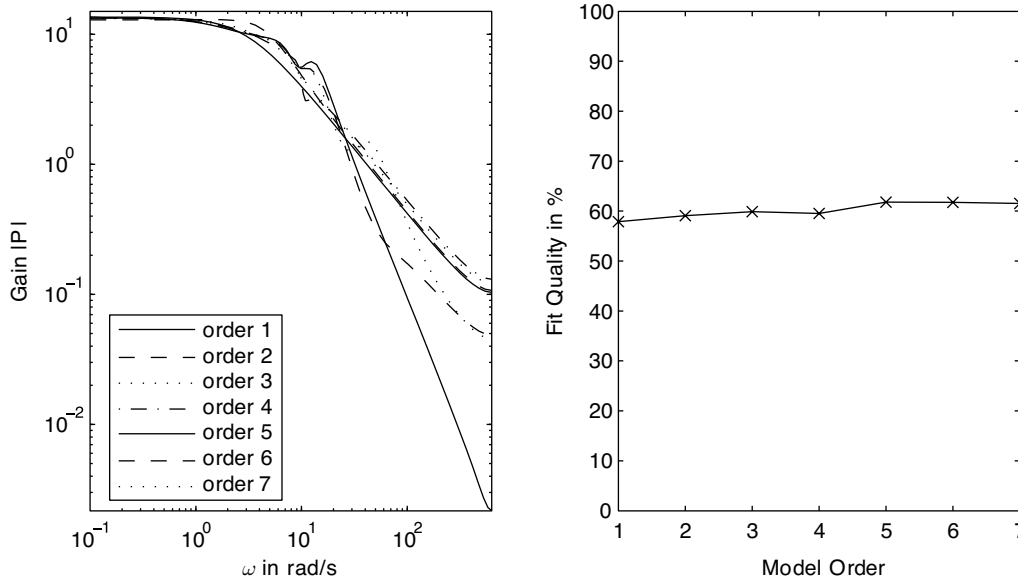


Figure 11: Identified models at one operating point ($\alpha = 4^\circ$, $\delta_f = 45^\circ$, $u_- = 2V$, $u_+ = 8V$) for model orders one to seven with respective quality of fit, defined in eq. (1). All models show similar behaviour at lower frequencies and notable differences in high frequency regimes. Higher order models lead to a faster roll-off in the gain.

All fits are between 57.88% (first order model) and 61.8% (fifth order model) in this case and thus can be seen as equally appropriate. All models show the same behaviour for low frequencies and roughly the same bandwidth where the roll-off of the gain sets in. The differences in the high frequency regime are not important for the controller synthesis, since the gains are low and the controller will try to further attenuate signals in the high frequency regime, anyway. With the model order the controller order increases when using a H_∞ -synthesis to account for uncertainties. Therefore, lower order transfer functions are generally preferred. Hence, first order models were chosen here as members of the model family. Only for very few fits, models of second order were chosen when first order identification did not yield satisfactory results.

The system dynamics are only weakly depending on the operating point, with the base voltage u_- from which the actuation signal is perturbed being the variable with the strongest influence. Figure 12 shows the influence of the angle of attack α on the dynamics. The models identified all have a similar dynamic and the sub-families for each α have a similar spread, too.

In order to make sure that the dynamics identified are actually mostly due to the aerodynamic behaviour, the dynamics of the pressurized air supply system were analysed separately. It was found that they were considerably faster – by a factor of three to five – than the dynamics of the plant itself, hence the model family is depicting mostly the aerodynamical behaviour of the flow. Any dynamics of the pressurized air supply system would be found at higher frequencies, where the model family already shows lower gains and thus the air supply system is not able to dominate the dynamics of the entire system. Nevertheless, in a real application the models have to incorporate both the aerodynamic effects and the dynamics of the actuation system.

Out of this model family, a mean model – called the ‘nominal model’ P_n – was chosen, with the parameters $\tau_d = -150.1$, $\kappa_1 = 60030$ and $\kappa_2 = 4.895$. This model was used as a basis to construct an uncertainty model with a multiplicative uncertainty such that all identified models belong to the set $P_u = P_n(1 + \omega_i \Delta)$, where Δ is an uncertain element with $\|\Delta\|_\infty \leq 1$ and ω_i is the weight that bounds the amplitude difference between the nominal model P_n and the maximum gain of all models at a specified frequency. Here, $\|\Delta\|_\infty = 1$ represents all asymptotically stable proper systems with gain smaller or equal to 1, i.e., $\|\Delta\|_\infty = \sup_\omega |\Delta(j\omega)| \leq 1$. For more details concerning modeling of uncertain systems and robust controller synthesis the reader is referred to standard textbooks such as [27]. The weight ω_i is, just as P_n and the other system describing models, a transfer function.

Figure 13 shows the Nyquist diagram for positive frequencies of the uncertainty modeling, which plots $P(j\omega)$ for $\omega \in [0, \infty]$. Every Nyquist plot of every identified model is within the borders of the uncertainty region, depicted by the light gray area, illustrating that all identified P belong to the set P_u .

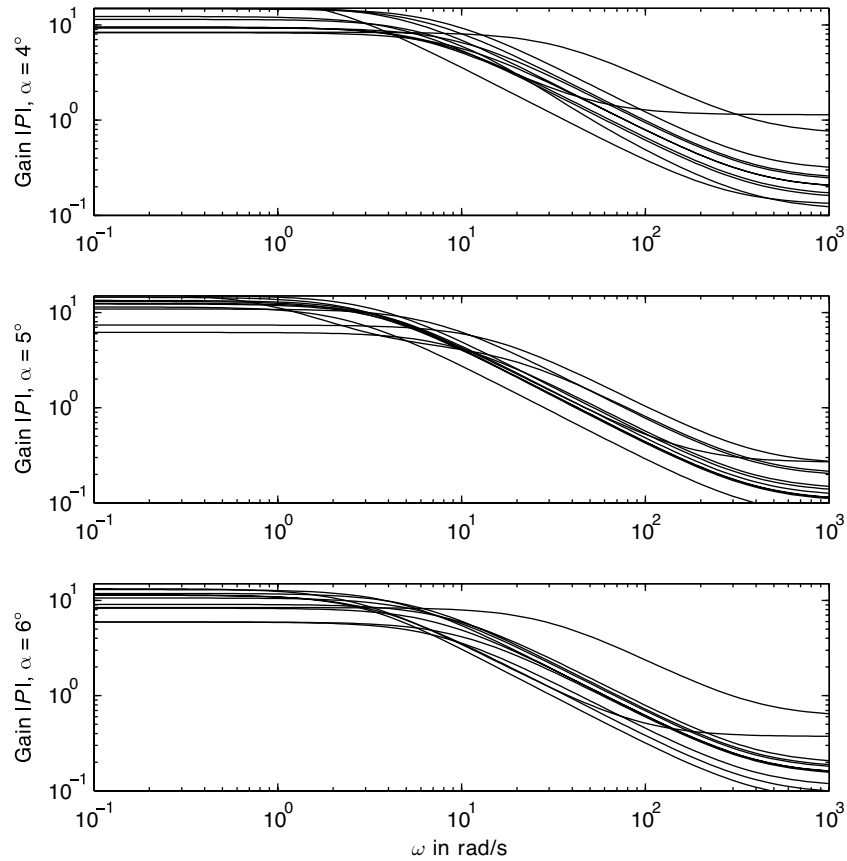


Figure 12: Sub-families of identified models for different α , showing basically similar dynamics and thus no strong dependence on the operating point α chosen. Different models of $\alpha = const.$ were obtained by varying u_- and u_+ .

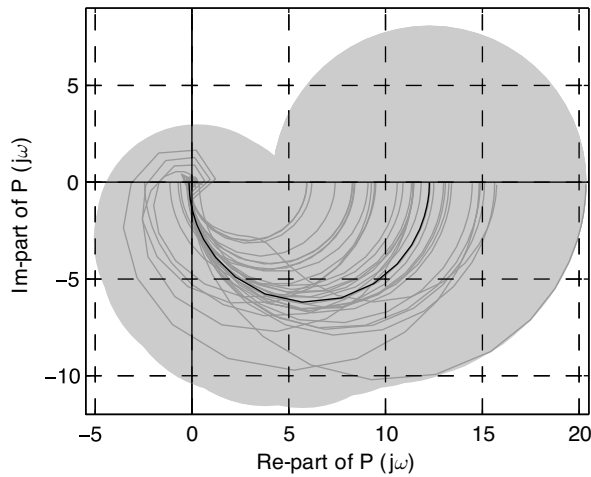


Figure 13: Nyquist diagram for all identified models (dark grey), the nominal model (black) and the uncertainty region (light grey area).

Controller Synthesis

Based on the nominal model, the open loop was shaped exploiting the Glover-McFarlane-algorithm [21],[22] to attain a robustified controller that is able to stabilize the closed loop and at the same time obtain some designer-specified characteristics. This method uses a pre-shaped open loop with the weights W_1 and W_2 to minimize the H_∞ -norm

$$\gamma := \min_{C_s} \left\| \begin{bmatrix} I \\ C \end{bmatrix} (I - PC)^{-1} [P, I] \right\|_{\infty} \quad (2)$$

where $C = W_2 C_s W_1$ is the controller transfer function with C_s as the optimization variable. In a first step, W_1 and W_2 are chosen in such a way, that the open-loop behaviour gets close to a desired open-loop behaviour, in this case the behaviour of an integrator to reduce the tracking error and achieve $\lim_{t \rightarrow \infty} (e) = 0$, with $e = l_{ref} - l$ being the tracking error, i.e., the difference between the set-point l_{ref} and the actual measurement l .

In a second step, the norm above is minimized to robustify the controller, i.e., make him as robust as possibly without changing the specified open-loop shape too much. Using a left-coprime factorisation, γ and therefore C_s can be calculated directly. For details of the calculation, the reader is referred to [21] and [22].

Thus, a controller was found with a maximum deviation between the loop-shapes of the first and second step of $1.42dB$, indicating that the robustification did in fact not change the open-loop shape significantly. This deviation exists only near the bandwidth frequency and is nearly zero at very high and very low frequencies, indicating the performance properties specified by the choice of W_1 and W_2 has been largely retained. Its Laplace-representation was

$$C = \frac{0.002s^3 + 0.2s^2 + 0.67s + 1.216}{s^4 + 79.07s^3 + 1678s^2 + 5104s} \quad (3)$$

This transfer function was then used to investigate the robust stability of the uncertain model to verify that this controller would stabilize every model family member.

The robust stability gain margin was 1.52, indicating that the uncertainty could be 52% larger than currently modeled, before the closed-loop would become unstable. This instability would then happen at a frequency of $\omega_c = 0.005 \frac{rad}{s}$. The magnitude of this stability margin applied to the uncertain object would lead to the sign of the gain response of P_u being unknown, i.e., the plant would begin to react contrarily to its normal behaviour in the face of actuation. For higher frequencies, the robust stability margin is increasing towards infinity. Since the uncertain model also models plants that will never be realized in reality, i.e., is too generous by nature, the controller found can be considered robustly stable.

Figure 14 shows the influence of one hundred samples of random variations in the uncertain parameters in Δ on the simulated tracking behaviour of the closed loop. As previously assumed, not one closed-loop is unstable and all of them tend towards $l = l_{ref}$, thus reducing the control error e .

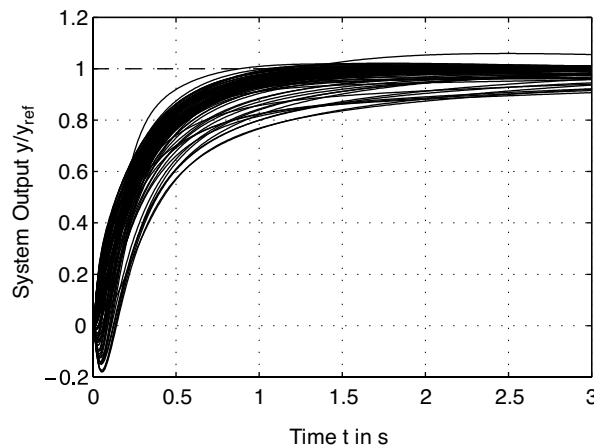


Figure 14: Randomly chosen plant models and their simulated tracking behaviour in the closed-loop set-up.

IV. EXPERIMENTAL CLOSED-LOOP CONTROL RESULTS

Closed-Loop Architecture

The controller found in section 3 was then used to set up a closed-loop experiment with an architecture as shown in Fig. 15.

The closed-loop set-up contains an anti-windup structure [23] to ascertain that the controller will not generate controller outputs that are not realisable, i.e., voltages corresponding to negative pressures or pressures above a maximum pressure dictated by the valve specifications. This anti-windup structure is a feedback loop for the regular controller, correcting its states in case the output signal u transgresses the minimal or maximal output values specified. This leads to the regular controller being able to work near the controller output signal limit without getting stuck there due to the integrator integrating a persistent tracking error up.

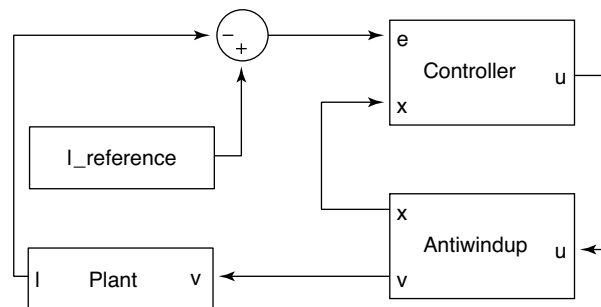


Figure 15: Closed-loop architecture for the controller validation.

There were no further digital filters involved, so the controller had to cope with a strongly noise-infested signal that was only filtered by the eigen-dynamics of the sensors. They basically constitute low-pass-filters of low order. In the following plots, however, for convenience and simplicity we will show digitally low-pass-filtered signals that were obtained in post-processing.

Disturbance Rejection

Since there was no way to induce reproducible disturbances into the wind-tunnel, the disturbance rejection has been judged indirectly.

Figure 16 shows a time-series of a closed-loop-experiment with the respective tracking error and the controller output signal. The controller was set to hold the present level of $l_{ref} = 480 \frac{N}{m}$. At $t = 2.6 s$ a spike in l occurs, indicating that the flow over the airfoil was suddenly reattaching, most likely due to an unknown disturbance in the wind-tunnel. Since we have set the controller to hold the level of l – here at a level that corresponds to a partly detached state – he begins shortly thereafter to lower the actuation pressure to make the flow separate again. While the flow responds to the controller output by driving l back towards the reference value, the controller gradually rises the pressure up again to hold the desired level of l . Within roughly $0.6 s$, the disturbance has been amended for. This is a proof of a good disturbance rejection.

On a further note, after the disturbance, the controller seems to get along with smaller outputs while still achieving the desired l_{ref} . This might be due to hysteresis effects or other non-linearities in the plant. The precise cause of this behaviour can not be erudated, but the point is, that the controller automatically choses the appropriate level of actuation to hold the desired l .

Figure 17 shows the pressure distribution over the flap at three distinct time points $t = 2.2 s$ (before the disturbance), $t = 2.6 s$ (at the disturbance peak) and $t = 3.4 s$ (after the disturbance). As discussed above, the disturbance improved the lift above the flap and with it above the wing. Pressure distributions are similar before and after the disturbance, indicating that the controller actually manages to indirectly shape the pressure distribution via l_{ref} .

Tracking Capability

Apart from holding a certain l_{ref} the capability to respond to changing l_{ref} -values was also examined, as shown in Fig. 18.

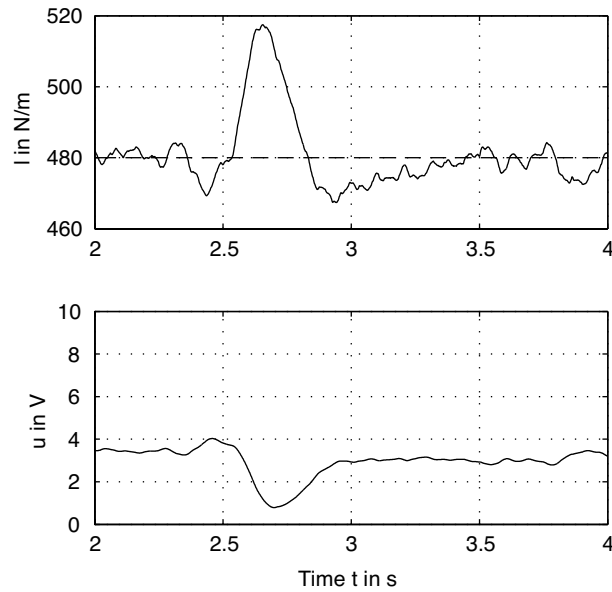


Figure 16: Disturbance rejection of the closed-loop set-up, showing l and l_{ref} and the corresponding controller output $u(t)$, at $\alpha = 4^\circ$, $Re_c = 10^6$, $DC_e = 50\%$, $f_e = 75$ Hz.

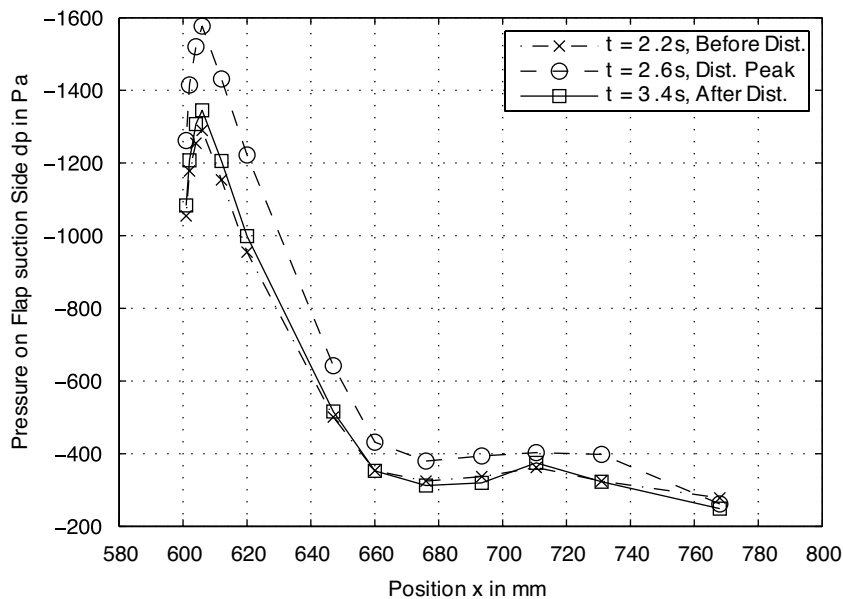


Figure 17: Pressure distribution at distinct time-points of the time-series shown in Fig. 16.

At $t = 7.1$ s and $t = 12.3$ s, l_{ref} was changed step-wise from $480 \frac{N}{m}$ to $520 \frac{N}{m}$ and back again, respectively. In both incidents, l was able to follow the new reference value within 0.3 s, with this delay being partly due to data shown here being filtered and partly due to the controller and plant properties.

This behaviour was reproducible at different operation points, differing in angle-of-attack α , the Re_c -number of the flow and the base actuation level or reference values l_{ref} . Even in flow regimes where the flow was unstable, i.e., alternating between separated and attached state, the controller was able to maintain a desired level for l .

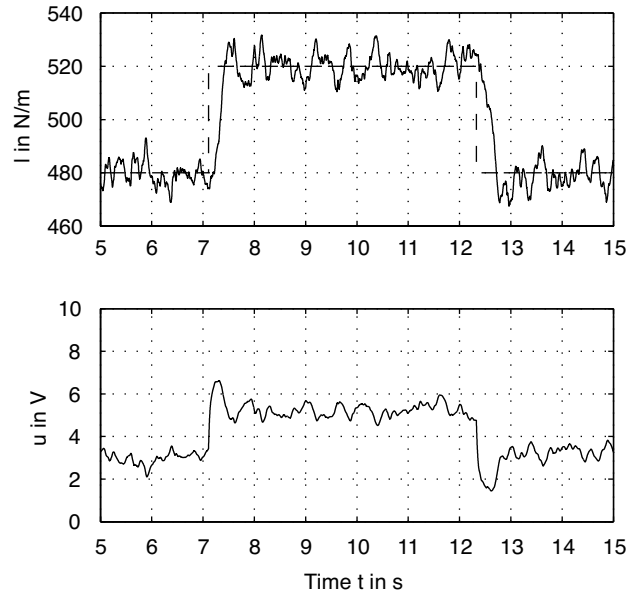


Figure 18: Tracking capability of the closed-loop set-up, showing I and the reference value I_{ref} (–) and the corresponding controller output $u(t)$, at $\alpha = 4^\circ$, $Re_c = 10^6$, $DC_e = 50\%$, $f_e = 75$ Hz.

V. SENSOR REQUIREMENTS

In the current set-up, 32 of the 49 sensors present are integrated over the chord length of the wing and the flap, all 32 being positioned on the suction side. For an industrial set-up, this number would have to be reduced due to restricted room in the wing as well as to cut costs and maintenance.

This reduction should not go at the expense of the measurements precision, so it boils down to the question of how many sensors are needed to accurately display the lift force L .

Principal component analysis (PCA) is one way to identify the most important elements of a measurement vector. There, a measurement matrix M is built from the measurements of the time-averaged pressure distribution at different angle-of-attacks and different actuating levels, where the pressure values at this operating point come as a row vector. M has to have a zero column mean.

From M , a singular value decomposition delivers $M = U\Sigma V^T$, where V^T contains the eigenvectors of the output space of M as row vectors and Σ contains the corresponding sorted singular values which weight the eigenvectors. The entries are sorted in descending order, so that $\sigma_i > \sigma_{i+1}$. Now, an arbitrary boundary between 0 and 1 is chosen and a value n calculated, such that the sum $\sum_{i=1}^n \sigma_i / \sum_{i=1}^N \sigma_i$ is smaller than that boundary, where N is the number of sensors available. Basically, this boundary indirectly determines the size of the reduced data space.

From V , the first n column vectors are chosen to comprise \bar{V} , the reduced eigenvector matrix.

$X = M\bar{V}$ yields the principal axis transformation of M onto the reduced set of principal axes. When assuming that the lift L is attainable through a linear combination of all sensor data, we get the ansatz $L = X\varphi$, where φ is the parameter vector. We then find that

$$\varphi = (X^T X)^{-1} X^T L \quad (4)$$

with φ now holding the parameter values for the principal axes and $\bar{V}\varphi$ therefore holding the parameter values for the underlying sensor data.

By beginning with the full set of sensors and examining the contribution of every sensor, eliminating the one with the smallest contribution to L , one can reduce the sensor set down to a smaller number which is able to represent most of the lift force L .

The steps lined out above will have to be repeated for every new reduced set of sensors, since the remaining sensors and their parameters will have to be readjusted to compensate for the contribution of the sensor that was eliminated.

With this method, different sets of time-averaged measurements were examined. During one set, α was changed step-wise from 0° to post-stall angles. The sets differed in the level of excitation. Several viable sensor set-ups were found. The smallest sensor set-up to deliver a maximum mean error of under 1% in any given set (0.95% for the case with maximum actuation) consisted of only four sensors. The mean error above all sets was at 0.65%. Three sensors lay on the suction side of the main element, spaced between $x/c = 0.093$ and $x/c = 0.645$ while the fourth sensor was located on the pressure side at $x/c = 0.002$.

The best overall set-up needed seven sensors, all on the main element spaced rather evenly from $x/c = 0$ to $x/c = 0.64$. This set-up showed a mean error of 0.63% and a maximum error of 1.0% again for the case with maximum actuation.

It has to be noted that for calculating the error and evaluating the quality of the fit, only the linear regime of the polar diagrams was considered. The fit becomes worse in the post-stall region, but this is – from a control-point of view – not important. A controller is designed to work in areas where the airfoil is expected to operate and there is no reason to operate it in post-stall areas. In fact, this is forbidden for commercial aircrafts. Still, even if the airfoil stalls, the set-up with seven sensors provides a reasonable good fit for the controller to work.

Figure 19 shows polar diagrams comparing L measured with a balance to L calculated, using the data from the best sensor set identified (see above). The polar curves differ in terms of actuation levels applied during the measurement.

This fit was even better than simply integrating the sensor data over the chord length as done in chapter 3, because it was able to compensate the changing angles of attack by hiding their effect in the weights given to the sensors. The problems shown in Fig. 7 do not apply anymore. Now there is a very close and linear equivalence between sensor data and L and a look-up-table is not necessary anymore.

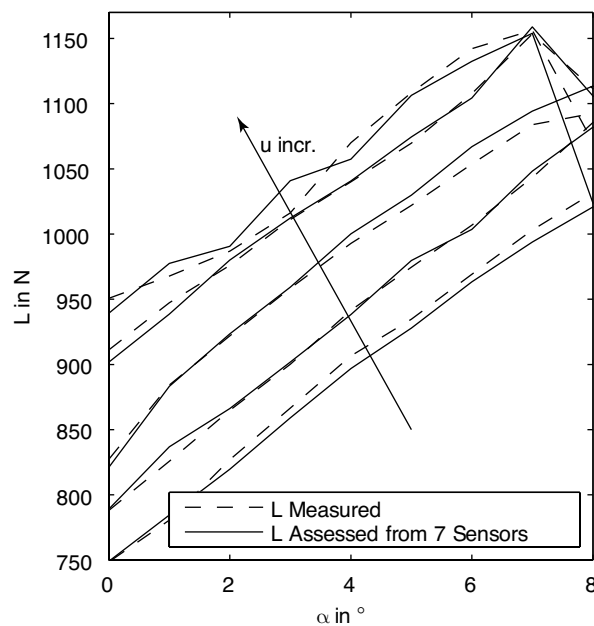


Figure 19: Polar diagrams to compare L measured with a balance to L calculated from seven pressure taps. The polar curves differ in terms of actuation levels during the measurement ($u = 0, 2, 4, 6, 8$ V).

VI. CONCLUSION

This work has shown that it is possible to derive a black-box-model for the lift over an high-lift configuration that was influenced by active flow control. From that model a closed-loop controller was designed and implemented. No in-depth physical knowledge was necessary for that implementation. The controller was derived by using the McFarlane-Glover-algorithm. It showed a good disturbance rejection and tracking capability over a wide span of operating points and was proven to be robustly stable, i.e., there is no operating point, at which the controller would destabilize the system, even when using an over-cautious worst-case uncertain model to test that robustness.

By examining the number and location of sensors needed to be able to accurately predict L , it was found that a small number of four to seven sensors on the main element suffices and is even more accurate than integrating the large number of sensors.

The approach proposed could be used to implement flight-stabilizing active flow control, where the pilot commands a certain lift he wishes to achieve at a certain angle-of-attack and the controller adjusts the actuation level in a way that the commanded lift is achieved. In case of a gust disturbing the flow around the airfoil, the controller could cancel out the effects of the gust by adjusting the actuation level accordingly. With further refinement [12], this could be done with separate segments on the wing so that the controller can even react to a local disturbance. Further possible benefits include enhanced maneuverability as well as a loss of weight and reduced fuel consumption with AFC-aware design of wings.

ACKNOWLEDGMENTS

This work was supported by the Deutsche Forschungsgemeinschaft (DFG, German Research Foundation) through the Collaborative Research Centre (SFB 557) 'Control of complex turbulent shear flows'.

REFERENCES

1. J. B. Barlow, W. H. Rae, and A. Pope. *Low Speed Wind Tunnel Testing*. John Wiley & Sons, Inc., 1999.
2. R. Becker, R. King, R. Petz, and W. Nitsche. Adaptive closed-loop separation control on a high-lift configuration using extremum seeking. *AIAA Journal*, 45(6):1382–1392, 2007.
3. D. P. Brzozowski, J. R. Culp, A. T. Kutay, J. A. Muse, and A. Glezer. Closed-Loop Aerodynamic Flow Control of a Free Airfoil. *AIAA 2008-4323*, 2008.
4. A. B. Cain, T. T. Ng, E. J. Kerschen, H. F. Fasel, and E. D. Fasse. *Flight Demonstration of Stealthy Closed-Loop Attitude Control*. Defense Technical Information Center, 2002.
5. M. Ciuryla, Y. Liu, J. Farnsworth, C. Kwan, and M. Amitay. Flight control using synthetic jets on a Cessna 182 model. *Journal of Aircraft*, 44(2):642, 2007.
6. M. E. DeSalvo and A. Glezer. Airfoil Aerodynamic Performance Modification using Hybrid Surface Actuators. *AIAA 2005-872*, 2005.
7. M. Gad-el Hak and D. M. Bushnell. Separation control: review. *Journal of Fluids Engineering*, 113(1):5–30, 1991.
8. B. Goeksel, I. Rechenberg, D. Greenblatt, and C. Paschereit. Steady and unsteady plasma wall jets for separation and circulation control. *AIAA 2006-3686*, 2006.
9. D. Greenblatt and I. J. Wygnanski. The control of flow separation by periodic excitation. *Progress in Aerospace Sciences*, 36(7):487–545, 2000.
10. F. Haucke, M. Bauer, T. Grund, W. Nitsche, and B. Gölling. An active flow control strategy for high-lift flaps. In *KATnet 2009, Bremen*, 2009.
11. F. Haucke, I. Peltzer, and W. Nitsche. Active separation control on a slatless 2d high-lift wing section. In *Proc. of the 26th ICAS Congress (ICAS-2008-175)*, pages ICAS-2008-175, 2008.
12. N. Heinz, R. King, M. Bauer, W. Nitsche, and B. Gölling. Robust closed-loop lift control on an industry-relevant civil aircraft half model. In R. King, editor, *Active Flow Control II*, pages 125–139. Springer Berlin, 2010.
13. L. Henning, R. Becker, G. Feuerbach, R. Muminovic, R. King, A. Brunn, and W. Nitsche. Extensions of adaptive slope-seeking for active flow control. *Proceedings of the Institution of Mechanical Engineers, Part I: Journal of Systems and Control Engineering*, 222(5):309–322, 2008.
14. W. B. Herbst. Dynamics of air combat. *Journal of Aircraft*, 20(7):594–598, 1983.
15. R. King, K. Aleksic, G. Gelbert, N. Losse, R. Muminovic, A. Brunn, W. Nitsche, M. R. Bothien, J. P. Moeck, C. O. Paschereit, B. R. Noack, U. Rist, and M. Zengl. Model predictive flow control. *AIAA 2008-3975*, 2008.
16. R. King, R. Becker, M. Garwon, and L. Henning. Robust and adaptive closed-loop control of separated shear flows. *AIAA 2004-2519*, 2004.
17. G. V. Lachmann. *Boundary layer and flow control: its principles and application*. Pergamon Press, 1961.

18. L. Ljung and E. J. Ljung. *System identification: theory for the user*. Prentice-Hall Englewood Cliffs, NJ, 1987.
19. D. M. Luchtenburg, K. Aleksic, M. Schlegel, B. R. Noack, King R., G. Tadmor, B. Gtinther, and F. Thiele. Turbulence control based on reduced-order models and nonlinear control design. In R. King, editor, *Active Flow Control II*, pages 341–356. Springer Berlin, 2010.
20. B. H. Maines, B. R. Smith, D. Merrill, S. Saddoughi, and H. Gonzalez. Synthetic Jet Flow Separation Control for Thin Wing Fighter Aircraft. *AIAA 2009-885*, 2009.
21. D. C. McFarlane and K. Glover. A loop-shaping design procedure using H_∞ synthesis. *IEEE Transactions on Automatic Control*, 37(6):759–769, 1992.
22. D. C. McFarlane and K. Glover. Robust controller design using normalized coprime factor plant descriptions. Springer New York, 1990.
23. J. K. Park and C. H. Choi. Dynamic compensation method for multi-variable control systems with saturating actuators. *IEEE Transactions on Automatic Control*, 40(9):1635–1640, 1995.
24. M. Pastoor, L. Henning, B. R. Noack, R. King, and G. Tadmor. Feedback shear layer control for bluff body drag reduction. *Journal of Fluid Mechanics*, 608:161–196, 2008.
25. L. Prandtl. Über Fliissigkeitsbewegung bei sehr kleiner Reibung (‘On Fluid Motion with Very Small Friction.’). *Verhandl. d. III Intl. Math. Kongr., Heidelberg, Germany (also NACA Tech. Memo)*, 452, 1928.
26. L. L. Shaw, B. R. Smith, and S. Saddoughi. Full-scale flight demonstration of active control of a pod wake. *AIAA 2006-3185*, 2006.
27. S. Skogestad and I. Postlethwaite. *Multivariable feedback control: analysis and design*. Wiley New York, 2007.
28. B. L. Smith and A. Glezer. The formation and evolution of synthetic jets. *Physics of Fluids*, 10:2281, 1998.
29. A. A. Tchieu, A. T. Kutay, J. A. Muse, A. J. Calise, and A. Leonard. Validation of a low-order model for closed-loop flow control enable flight. *AIAA 2008-3863*, 2008.
30. Y. Tian, Q. Song, and L. Cattafesta. Adaptive feedback control of flow separation. *AIAA 2006-3016*, 2006.
31. J. Wild, G. Wichmann, F. Haucke, I. Peltzer, and P. Scholz. Large scale separation flow control experiments within the German Flow Control Network. *AIAA 2009-530*, 2009.
32. D. Williams, W. Kerstens, J. Pfeiffer, R. King, and T. Colonius. Unsteady lift suppression with a robust closed loop controller. In R. King, editor, *Active Flow Control II*, pages 19–30. Springer Berlin, 2010.